Journal of Power Sources 196 (2011) 6332–6346

Contents lists available at ScienceDirect

Journal of Power Sources

journal homepage: www.elsevier.com/locate/jpowsour

Analysis of an active tubular liquid-feed direct methanol fuel cell

Chao Xu[1], Amir Faghri*

Department of Mechanical Engineering, University of Connecticut, Storrs, CT 06269, USA

ARTICLE INFO

Article history:
Received 3 February 2011
Accepted 18 March 2011
Available online 29 March 2011

Keywords:
Active DMFC
Tubular
Mass transport
Heat transport

ABSTRACT

A two-dimensional, two-phase, non-isothermal model was developed for an active, tubular, liquid-feed direct methanol fuel cell (DMFC). The liquid–gas, two-phase mass transport in the porous anode and cathode was formulated based on the multi-fluid approach in the porous media. The two-phase mass transport in the anode and cathode channels was modeled using the drift-flux and the homogeneous mist-flow models, respectively. Water and methanol crossovers through the membrane were considered due to the effects of diffusion, electro-osmotic drag, and convection. The model enabled a numerical investigation of the effects of various operating parameters, such as current density, methanol flow rate, and oxygen flow rate, on the mass and heat transport characteristics in the tubular DMFC. It was shown that by choosing a proper tube radius and distance between the adjacent cells, a tubular DMFC stack can achieve a much higher energy density compared to its planar counterpart. The results also showed that a large anode flow rate is needed in order to avoid severe blockage of liquid methanol to the anode electrode due to the gas accumulation in the channel. Besides, lowering the flow rate of either the methanol solution or air can lead to a temperature increase along the flow channel. The methanol and water crossovers are nearly independent of the methanol flow rate and the air flow rate.

1. Introduction

In the past decade, the direct methanol fuel cell (DMFC) has been extensively investigated as a promising power source candidate for electronic devices, such as laptops and portable digital assistants. The unique advantages of the DMFC include high energy density, low emission, instant recharging, and compact structure. However, the commercialization of the DMFC is still hindered by several technical problems, including the low electro-activity of methanol oxidation at the anode as well as methanol and water crossovers through the membrane [1–11]. Great efforts continue to be made to resolve these problems.

Previous DMFC research and development were mainly based on the planar cell structure [2–14], and relatively little work has been reported about the tubular DMFC [15–24], which is all experimental work. Compared to the planar cell structure, the tubular cell structure has some specific advantages, including:

(i) it has a larger electrode surface-to-volume ratio, and thus, a higher system energy density can be achieved;
(ii) it has a greater flexibility in shape;
(iii) it eliminates the need for additional plates on both the anode and the cathode sides to hold the structure together.

Due to these advantages, the tubular cell structure has been widely used in solid oxide fuel cells (SOFCs). However, the application of the tubular cell structure on low temperature fuel cells, such as polymer electrolyte fuel cells (PEFCs) and DMFCs, has rarely been reported.

Recently, some experimental work has been carried out to develop tubular DMFCs, with the efforts focusing mainly on the methods of fabricating the tubular membrane-electrode-assembly (MEA) and on the improvement of the cell performance. Kunimatsu and Okada [16] reported the performance of a tubular DMFC using a micro-tubular electrolyte. It was shown that both the catalyst layer fabrication and hot-pressing process were crucial to the tubular cell performance. A peak power density of 12 mW cm^{-2} was achieved with an air-breathing tubular DMFC fed with 1 M methanol solution, which indicated that in terms of power density, tubular DMFCs can perform as well as planar DMFCs. Qiao et al. [17–19] reported different methods for fabricating the tubular anode and cathode, including the impregnation-reduction method with heat treatment for the anode fabrication, impregnation-reduction method with a new plating process for the cathode fabrication, and a wet chemical assembling process for the formation of the anode. It was found

* Corresponding author at: Department of Mechanical Engineering, University of Connecticut, 191 Auditorium Road, Unit 3139, Storrs, CT 06269-3139, USA. Tel.: +1 860 486 0419; fax: +1 860 486 0479.
E-mail address: faghri@engr.uconn.edu (A. Faghri).
[1] Current address: Key Laboratory of Solar Thermal Energy and Photovoltaic System, Institute of Electrical Engineering, Chinese Academy of Sciences, Beijing 100190, PR China.

0378-7753/$ – see front matter © 2011 Elsevier B.V. All rights reserved.
doi:10.1016/j.jpowsour.2011.03.038

Nomenclature

A_{lg}	interfacial specific area between liquid and gas phase, $m^2\ m^{-3}$
A_v	specific area, $m^2\ m^{-3}$
a_w	water vapor activity
C	molar concentration, $mol\ m^{-3}$
c_p	specific heat capacity, $J\ kg^{-1}\ T^{-1}$
D	diffusivity, $m^2\ s^{-1}$
F	Faraday constant, 96,478 $C\ mol^{-1}$
Gr	Grashof number
h	heat transfer coefficient, $W\ m^{-1}\ K^{-1}$; enthalpy, $J\ mol^{-1}$
h_{lg}	interfacial transfer rate constant for methanol, $m^2\ s^{-1}$
h_m	mass transfer coefficient, $m^{-2}\ s^{-1}$
I	current density, $A\ m^{-2}$
I_p	parasitic current resulting from methanol crossover, $A\ m^{-2}$
J	molar flux, $mol\ m^{-2}\ s^{-1}$
j_0	exchange current density, $A\ m^{-2}$
j_a	anode current density, $A\ m^{-3}$
j_c	cathode current density, $A\ m^{-3}$
K	permeability of porous material, m^2
k	thermal conductivity, $W\ m^{-1}\ K^{-1}$
k_c	condensation rate, $mol\ (atm\ s\ m^3)^{-1}$
k_e	evaporation rate, $(atm\ s)^{-1}$
k_{rl}, k_{rg}	relative permeability
$\dot{m}$	source term in mass conservation equation, $kg\ m^{-3}\ s^{-1}$
m	mass flux, $kg\ m^{-2}\ s^{-1}$
M	molecular weight, $kg\ mol^{-1}$
N	mol flux, $mol\ m^{-2}\ s^{-1}$
n_d	electro-osmotic drag coefficient
p_c	capillary pressure, Pa
p_g	gas phase pressure, Pa
p_l	liquid phase pressure, Pa
q	heat flux, $W\ m^{-2}$
R	gas constant, $J\ (mol\ K)^{-1}$
$\dot{R}$	source term in species conservation equation, $mol\ m^{-3}\ s^{-1}$
$\tilde{R}$	interfacial species transfer rate, $mol\ m^{-3}\ s^{-1}$
$R_{contact}$	ohmic contact resistance, $\Omega\ m^2$
S	source term; entropy
s	liquid saturation; entropy
T	temperature, K
u, v	velocity, $m\ s^{-1}$
V_0	thermodynamic equilibrium voltage, V
V_{cell}	cell voltage, V
x	coordinate, m
r	coordinate, m

Greek

α_a	anode transfer coefficient at anode
α_c	cathode transfer coefficient at cathode
γ	reaction order of ORR
δ	thickness, m
ε	porosity of porous medium
η	overpotential, V
λ	water content
μ	viscosity, $kg\ m^{-1}\ s^{-1}$
ρ	density, $kg\ m^{-3}$
σ	interfacial tension, $N\ m^{-1}$; proton conductivity, $\Omega^{-1}\ m^{-1}$

Superscripts

eff	effective value
ref	reference value
sat	saturated value
*	in equilibrium

Subscripts

a	anode
c	cathode, or capillary
cr	crossover
dry	dry membrane
e	electrolyte, or evaporation
g	gas phase
l	liquid phase
mem	membrane
ML	methanol
MV	methanol vapor
p	parasitic
rl	relative value for liquid phase
rg	relative value for gas phase
T	temperature
W	water
we	dissolved water
WV	water vapor

that improving the fabrication process of the electrodes on the tubular membrane was effective to improve the tubular DMFC performance. Shao et al. [20,21] developed a new method to fabricate the tubular DMFC. A tubular titanium mesh was used to support the catalysts and collect the current from the cell. The catalyst layers were fabricated using a dip coating method—a recast Nafion membrane was coated on the cathode electrode. A dilute sulfuric acid solution was used as the electrolyte to reduce the contact resistance between the anode and the membrane. It was also shown that the tubular DMFC performed similar to the conventional planar DMFC. Yu et al. [23] used a porous silica pipe as the support to fabricate the tubular electrolyte membrane, on which they further investigated the cell performance of the tubular DMFC and tubular PEFC. Lee et al. [24] investigated the performance of a tubular DMFC, in which the tubular MEA was fabricated by curling the conventional MEA into a tube.

Like in the planar DMFC, a number of physicochemical phenomena take place in the tubular DMFC, including species transport, momentum transport, and multiple electrochemical reactions, of which a better understanding is essential to optimize the tubular cell structure and improve the cell performance. Extensive efforts have been made to develop two-phase mass transport models for planar DMFCs in order to quantify the complex transport phenomena and elucidate the mechanisms of different transport processes [11,12,25–31]. Wang and Wang [12] modeled the DMFC using the mixture multiphase flow model, in which the species in the liquid and gas phases were assumed to be at the thermodynamic equilibrium condition. Yang and Zhao [11,26] presented a two-phase mass transport model for the DMFC, which was developed based on the multiphase flow theory in porous media. Xu et al. [25] developed a one-dimensional, isothermal, two-phase mass transport model for the DMFC. The respective effects of three water transport mechanisms through the membrane, as well as the effect of the MEA design on the water crossover and cell performance, were investigated. Rice and Faghri [30] proposed a transient, two-dimensional, multi-phase model for a DMFC with a passive fuel delivery system. The passive delivery system utilized a porous medium to passively deliver methanol to the fuel

cell while controlling the concentration of methanol at the anode side to limit the amount of methanol crossover. Rice and Faghri [31] further developed a thermal model to study the thermal and start-up characteristics of a passive DMFC system. Their model also included continuous and discontinuous phase limitations, as well as a probabilistic spread of the porous properties. Recently, Xu and Faghri [3] investigated the water transport characteristics in a passive liquid-feed DMFC using a two-dimensional, two-phase, non-isothermal model. The effects of various operating parameters, such as current density, methanol concentration, and air humidity, as well as the effect of the cathode hydrophobic air filter layer, on the water transport and cell performance, were investigated.

However, with regard to tubular PEFCs and DMFCs, only one investigation about the modeling of tubular PEFCs was reported. Al-Baghdadi [32] developed a three-dimensional, non-isothermal, mass transport model of a tubular PEFC, which was used to understand the many physicochemical interactions, complex electrochemical reactions, and transport phenomena that cannot be studied experimentally. The model was also used to study the effects of various material parameters on the cell performance. To the authors' knowledge, no numerical work in relation to the tubular DMFC has been reported in the literature.

The objective of this work was to develop a two-dimensional, non-isothermal, two-phase mass transport model for a tubular liquid-feed DMFC. The liquid–gas, two-phase mass transport in the porous anode and cathode was formulated based on the multi-fluid model in the porous media, and the two-phase mass transport in the anode and cathode channels was modeled using the drift-flux and the homogeneous mist-flow models, respectively. Since the micro-porous layers (MPLs) play an important role in fuel and water management, this model also includes MPLs between the diffusion and catalyst layers of both the anode and the cathode. Firstly, an evaluation of the advantage of a tubular DMFC system in terms of energy density compared to a planar system was presented. Then, the model developments of the tubular DMFC and the numerical results obtained were introduced. Both the mass transport characteristics and the heat behavior of the tubular DMFC, with different current densities and fuel and oxygen flow rates, were investigated.

2. Energy density evaluation of the tubular DMFC

The energy density of a DMFC stack can be increased by increasing the reactive surface area per unit volume. For a tubular DMFC stack, the reactive surface area depends greatly on the geometry size of the unit tubular cell, particularly the radius of the tube channel. To elucidate the benefit of a tubular DMFC stack versus a planar stack with regards to the energy density, the reactive surface areas per unit volume were evaluated for each.

Consider a standard planar DMFC stack, as shown in Fig. 1a, having a cross-sectional area of W (width) $\times$ H (height) and a length of L. The total cell number can be approximated by $H/(T_{MEA} + T_{BP})$, where T_{MEA} is the thickness of the MEA, and T_{BP} is the thickness of the bipolar plate. Thus, the reactive surface area corresponding to the unit stack volume is $W \times L \times (H/(T_{MEA} + T_{BP}))$. While for a unit tubular DMFC stack, which has the same volume size as the standard planar stack, the total cell number depends on both the tube size and distance between the tubes. Assuming the shortest distance between the electrodes of two adjacent tubular cells is n times the radius of the inner tubular channel (R), as shown in Fig. 1b, the total cell number can be expressed by $W \times H/(2R + nR + 2T_{MEA})^2$. Thus, the reactive surface area corresponding to the unit stack volume is $\pi \times (2R + T_{MEA}) \times (W \times H/(2R + nR + 2T_{MEA})^2)$.

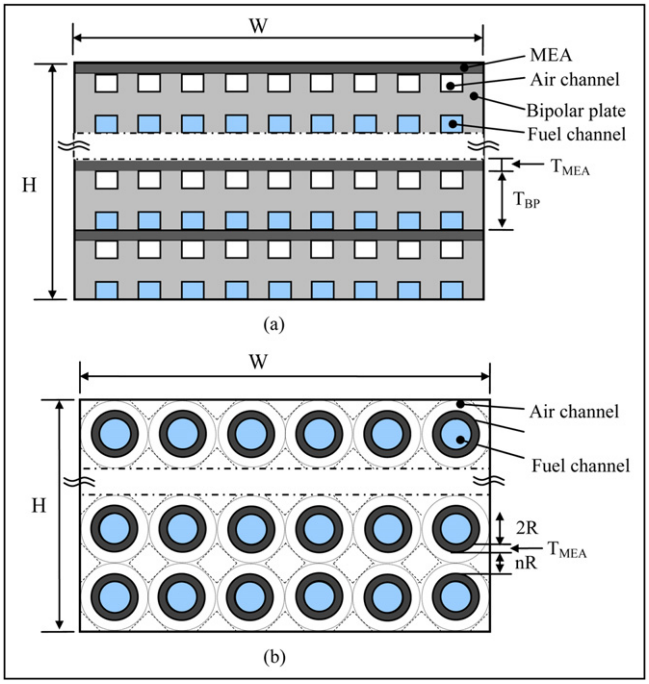

Fig. 1. Sectional views of (a) a planar fuel cell stack and (b) a tubular fuel cell stack.

Accordingly, the ratio of the reactive surface area of the tubular fuel cell stack to the planar fuel cell stack is:

$$\frac{\pi \times (2R + T_{MEA}) \times L \times (W \times H/(2R + nR + 2T_{MEA})^2)}{W \times L \times (H/(T_{MEA} + T_{BP}))} = \frac{\pi \times (T_{MEA} + T_{BP}) \times (2R + T_{MEA})}{(2R + nR + 2T_{MEA})^2} \quad (1)$$

For a standard planar fuel cell, the thicknesses of the bipolar plate and MEA are about 3 mm and 0.6 mm, respectively. Fig. 2 shows the variation in the ratio of the reactive surface area, which indicates the ratio of the stack energy density when the cell performance of a unit area in the planar and the tubular stack is assumed to be the same.

It is seen that the ratio depends on both the tube radius and distance between the adjacent tubular cells. For instance, when

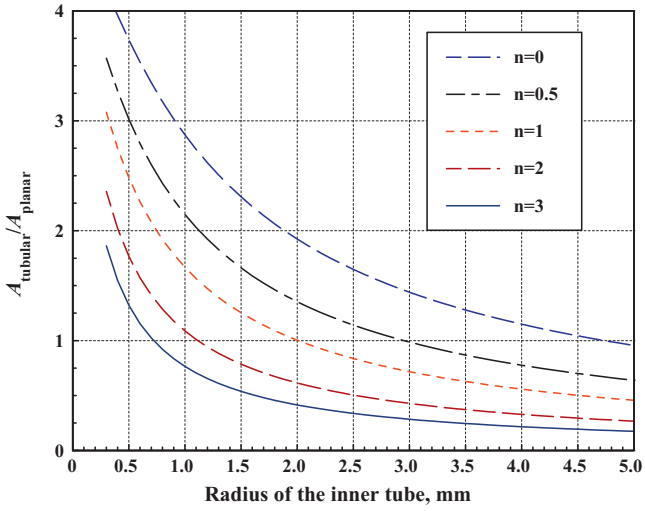

Fig. 2. Variation of the ratio of the reactive surface area of a tubular fuel cell stack to a planar fuel cell stack which have the same volume (assume: T_{MEA} = 0.6 mm; T_{BP} = 3 mm).

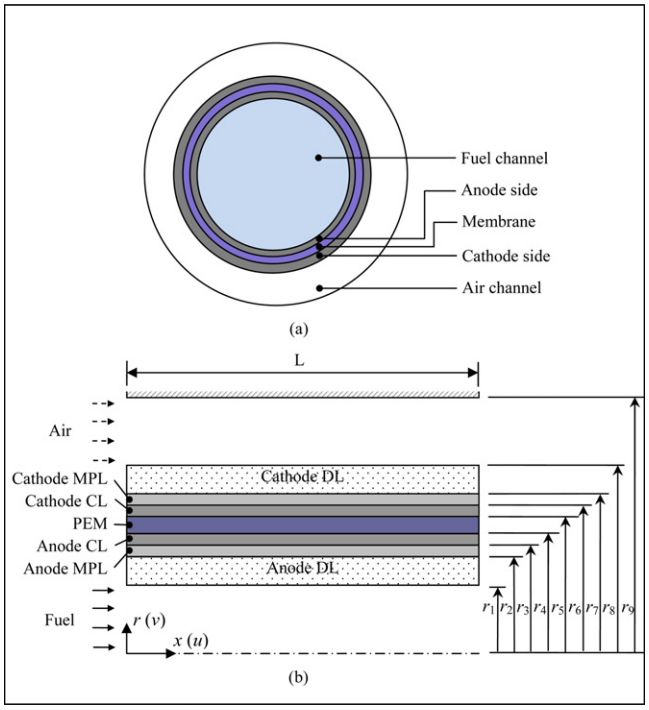

Fig. 3. (a) Schematic of a tubular DMFC cross-section and (b) the computational domain.

$n = 1$, the ratio first decreases sharply and then slowly continues to decrease with an increase in the tube radius. When the radius becomes a critical value of 2.0 mm, the ratio is 1.0, which means that the reactive surface areas are the same for both the tubular and planar stacks. When the radius is larger than the critical value (2.0 mm), the reactive surface area of the tubular stack, as well as the energy density, is less than that of the planar one. With a decrease in the distance between adjacent tubular cells, the critical value is increased. When $n = 0$, which means the adjacent tubular cells come into contact, the critical value increases to about 4.7 mm. Therefore, to achieve a higher energy density when using a tubular DMFC stack, both the tube radius and distance between the adjacent cells should be considered.

3. Model formulation

This section presents a comprehensive steady state, two-dimensional, two-phase, non-isothermal model of a tubular-shaped DMFC, as illustrated in Fig. 3. The tubular DMFC includes an anode flow channel (ACF) inside the tubular cell, anode diffusion layer (DL), anode micro-porous layer (MPL), anode catalyst layer (CL), polymer electrolyte membrane (PEM), cathode CL, cathode MPL, cathode DL, and an annular cathode flow channel (CFC) outside of the tubular cell. The following presents the model to formulate the mass and heat transport in different regions of the computational domain. The following main assumptions were made in the model:

(i) The flow is symmetrical about the axis. Therefore, all $\partial/\partial\theta$ terms are neglected in the governing equations, and the governing equations for transport within the MEA become two-dimensional.
(ii) Two phase flow in the anode and cathode channels are based on one-dimensional drift-flux flow and homogeneous flow along the direction of the channel, respectively.
(iii) The porous layers are homogeneous and isotropic.
(iv) Both the gas and liquid phases are continuous in the porous layers, and the flows of gas and liquid are all controlled by Darcy's law.
(v) Only water and methanol are considered the condensable species.
(vi) The membrane is impermeable to both gas and liquid, and only dissolved methanol and water can crossover through the membrane.
(vii) The liquid and gas phase temperatures are the same.

3.1. Transport multiple governing equations

3.1.1. Mass transport in the anode porous region

The anode porous region includes the anode DL, anode MPL, and anode CL. Due to the coexistence of hydrophilic and hydrophobic pores, both liquid and gas phases exist in the porous region. The general governing equations of the mass and momentum conservation corresponding to each phase, as well as the conservation of species, are given by:

$$\textbf{Mass}: \quad \nabla\cdot\left[\rho_l\vec{u}_l\right] = \frac{\partial(\rho_l u_l)}{\partial x} + \frac{1}{r}\frac{\partial(r\rho_l v_l)}{\partial r} = \dot{m}_{l,a} \quad \text{(liquid phase)} \tag{2}$$

$$\nabla\cdot\left[\rho_g\vec{u}_g\right] = \frac{\partial(\rho_g u_g)}{\partial x} + \frac{1}{r}\frac{\partial(r\rho_g v_g)}{\partial r} = \dot{m}_{g,a} \quad \text{(gas phase)} \tag{3}$$

where $\vec{u} = u\mathbf{i} + v\mathbf{k}$ represents the superficial velocity vector based on the total cross-sectional area of the fluids and porous medium. The rate of mass generation is represented by $\dot{m}$.

$$\textbf{Momentum}: \quad \vec{u}_l = -K\frac{k_{rl}}{\mu_l}\nabla p_{l,a} \quad \text{(liquid phase)} \tag{4}$$

$$\vec{u}_g = -K\frac{k_{rg}}{\mu_g}\nabla p_{g,a} \quad \text{(gas phase)} \tag{5}$$

where K is the intrinsic permeability of the porous medium and k_r denotes the relative permeability of the phase.

Substituting Eqs. (4) and (5) into Eqs. (2) and (3), respectively, yields the governing equations for the anode liquid pressure ($p_{l,a}$) and gas pressure ($p_{g,a}$):

$$-\frac{\partial}{\partial x}\left(\frac{\rho_l K k_{rl}}{\mu_l}\frac{\partial p_{l,a}}{\partial x}\right) - \frac{1}{r}\frac{\partial}{\partial r}\left(r\frac{\rho_l K k_{rl}}{\mu_l}\frac{\partial p_{l,a}}{\partial r}\right) = \dot{m}_{l,a} \tag{6}$$

$$-\frac{\partial}{\partial x}\left(\frac{\rho_g K k_{rg}}{\mu_g}\frac{\partial p_{g,a}}{\partial x}\right) - \frac{1}{r}\frac{\partial}{\partial r}\left(r\frac{\rho_g K k_{rg}}{\mu_l}\frac{\partial p_{g,a}}{\partial r}\right) = \dot{m}_{g,a} \tag{7}$$

$$\textbf{Species}: \quad \frac{\partial(u_l C_{ML,a})}{\partial x} + \frac{1}{r}\frac{\partial(rv_l C_{ML,a})}{\partial r} = \frac{\partial}{\partial x}\left(D^{eff}_{ML,a}\frac{\partial C_{ML,a}}{\partial x}\right) + \frac{1}{r}\frac{\partial}{\partial r}\left(rD^{eff}_{ML,a}\frac{\partial C_{ML,a}}{\partial r}\right) + \dot{R}_{ML,a} \tag{8}$$

$$\frac{\partial(u_g C_{MV,ga})}{\partial x} + \frac{1}{r}\frac{\partial(rv_g C_{MV,ga})}{\partial r} = \frac{\partial}{\partial x}\left(D^{eff}_{MV,ga}\frac{\partial C_{MV,ga}}{\partial x}\right) + \frac{1}{r}\frac{\partial}{\partial r}\left(rD^{eff}_{MV,ga}\frac{\partial C_{MV,ga}}{\partial r}\right) + \dot{R}_{MV,ga} \tag{9}$$

$$\frac{\partial(u_g C_{WV,ga})}{\partial x} + \frac{1}{r}\frac{\partial(rv_g C_{WV,ga})}{\partial r} = \frac{\partial}{\partial x}\left(D^{eff}_{WV,ga}\frac{\partial C_{WV,ga}}{\partial x}\right) + \frac{1}{r}\frac{\partial}{\partial r}\left(rD^{eff}_{WV,ga}\frac{\partial C_{WV,ga}}{\partial r}\right) + \dot{R}_{WV,ga} \tag{10}$$

where $C_{ML,a}$, $C_{MV,ga}$, and $C_{WV,ga}$ are the liquid methanol concentration, methanol vapor concentration, and water vapor concentration

in the anode side, respectively. D_i^{eff} represents the effective diffusion coefficient of species i and $\dot{R}_i$ denotes the mole generation rate of species i.

3.1.2. Mass transport in the cathode porous region

Similar to the anode porous region, both liquid and gas phases exist in the cathode porous region which includes the cathode DL, cathode MPL, and cathode CL. The general governing equations of the mass and momentum conservation corresponding to each phase, as well as the conservation of species, are given by:

$$\textbf{Mass}: \quad \nabla\cdot\left[\rho_{\text{l}}\vec{u}_{\text{l}}\right]=\frac{\partial(\rho_{\text{l}}u_{\text{l}})}{\partial x}+\frac{1}{r}\frac{\partial(r\rho_{\text{l}}v_{\text{l}})}{\partial r}=\dot{m}_{\text{l,c}} \quad \text{(liquid phase)} \tag{11}$$

$$\nabla\cdot\left[\rho_{\text{g}}\vec{u}_{\text{g}}\right]=\frac{\partial(\rho_{\text{g}}u_{\text{g}})}{\partial x}+\frac{1}{r}\frac{\partial(r\rho_{\text{g}}v_{\text{g}})}{\partial r}=\dot{m}_{\text{g,c}} \quad \text{(gas phase)} \tag{12}$$

$$\textbf{Momentum}: \quad \vec{u}_{\text{l}}=-K\frac{k_{\text{rl}}}{\mu_{\text{l}}}\nabla p_{\text{l,c}} \quad \text{(liquid phase)} \tag{13}$$

$$\vec{u}_{\text{g}}=-K\frac{k_{\text{rg}}}{\mu_{\text{g}}}\nabla p_{\text{g,c}} \quad \text{(gas phase)} \tag{14}$$

Similarly, the governing equations for the cathode liquid pressure ($p_{\text{l,c}}$) and gas pressure ($p_{\text{g,c}}$) can be obtained from Eqs. (11)–(14), which give:

$$-\frac{\partial}{\partial x}\left(\frac{\rho_{\text{l}}Kk_{\text{rl}}}{\mu_{\text{l}}}\frac{\partial p_{\text{l,c}}}{\partial x}\right)-\frac{1}{r}\frac{\partial}{\partial r}\left(r\frac{\rho_{\text{l}}Kk_{\text{rl}}}{\mu_{\text{l}}}\frac{\partial p_{\text{l,c}}}{\partial r}\right)=\dot{m}_{\text{l,c}} \tag{15}$$

$$-\frac{\partial}{\partial x}\left(\frac{\rho_{\text{g}}Kk_{\text{rg}}}{\mu_{\text{g}}}\frac{\partial p_{\text{g,c}}}{\partial x}\right)-\frac{1}{r}\frac{\partial}{\partial r}\left(r\frac{\rho_{\text{g}}Kk_{\text{rg}}}{\mu_{\text{l}}}\frac{\partial p_{\text{g,c}}}{\partial r}\right)=\dot{m}_{\text{g,c}} \tag{16}$$

$$\textbf{Species}: \quad \frac{\partial(u_{\text{g}}C_{\text{O}_2,\text{gc}})}{\partial x}+\frac{1}{r}\frac{\partial(rv_{\text{g}}C_{\text{O}_2,\text{gc}})}{\partial r}=\frac{\partial}{\partial x}\left(D^{\text{eff}}_{\text{O}_2,\text{gc}}\frac{\partial C_{\text{O}_2,\text{gc}}}{\partial x}\right)+\frac{1}{r}\frac{\partial}{\partial r}\left(rD^{\text{eff}}_{\text{ML,a}}\frac{\partial C_{\text{O}_2,\text{gc}}}{\partial r}\right)+\dot{R}_{\text{O}_2,\text{gc}} \tag{17}$$

$$\frac{\partial(u_{\text{g}}C_{\text{WV,gc}})}{\partial x}+\frac{1}{r}\frac{\partial(rv_{\text{g}}C_{\text{WV,gc}})}{\partial r}=\frac{\partial}{\partial x}\left(D^{\text{eff}}_{\text{WV,gc}}\frac{\partial C_{\text{WV,gc}}}{\partial x}\right)+\frac{1}{r}\frac{\partial}{\partial r}\left(rD^{\text{eff}}_{\text{WV,ga}}\frac{\partial C_{\text{WV,gc}}}{\partial r}\right)+\dot{R}_{\text{WV,gc}} \tag{18}$$

where $C_{\text{O}_2,\text{gc}}$ and $C_{\text{WV,gc}}$ are the gas oxygen concentration and water vapor concentration in the cathode side, respectively.

Here it should be noted that the capillary pressure for the porous region is given by [33]:

$$p_{\text{c}}=p_{\text{g}}-p_{\text{l}}=\sigma\cos\theta(\varepsilon/K)^{0.5}J(s) \tag{19}$$

where $J(s)$ represents the widely used Leverett function:

$$J(s)=\begin{cases}1.417(1-s)-2.120(1-s)^2+1.263(1-s)^3 & 0<\theta\le 90^\circ\\ 1.417s-2.120s^2+1.263s^3 & 90^\circ<\theta<180^\circ\end{cases} \tag{20}$$

When the gas and liquid pressures are solved in every iteration, the liquid saturation is determined by Eqs. (19) and (20). Recently, some efforts have been devoted toward the determination of the capillary property of the fuel cell porous media. However, there are inconsistencies in the newly developed capillary functions, and thus, the Leverett function is still used in this work [34].

3.1.3. Mass transport in the membrane

Due to its extremely low permeability, the membrane is usually regarded as a gas insulator. However, liquid water and methanol in the porous region can dissolve into the electrolyte with the effect of adsorption to form the dissolved phase and cause transport between the anode and cathode through the membrane. The transfer of the dissolved water through the membrane depends on molecular diffusion, electro-osmotic drag and convection. Accordingly, the molar flux of water crossover ($N_{\text{H}_2\text{Ocr}}$) through the membrane can be given by:

$$N_{\text{H}_2\text{Ocr}}=-D_{\text{we}}(\lambda)\nabla C_{\text{we}}+n_{\text{d,H}_2\text{O}}\frac{I}{F}-\frac{K_{\text{mem}}\rho_{\text{l}}}{\mu_{\text{l}}M_{\text{H}_2\text{O}}}\nabla p_{\text{l}} \tag{21}$$

Thus, the governing equation for the dissolved water concentration (C_{we}) is:

$$\nabla\cdot N_{\text{H}_2\text{Ocr}}=\nabla\cdot(-D_{\text{we}}(\lambda)\nabla C_{\text{we}})+\nabla\cdot\left(n_{\text{d,H}_2\text{O}}\frac{I}{F}\right)=0 \tag{22}$$

Note that the dissolved water concentration C_{we} can be transformed to the water content λ in the electrolyte and the relationship between C_{we} and λ is given by $\lambda = C_{\text{we}}(EW/\rho_{\text{dry}})$.

The molar flux of methanol crossover (N_{MLcr}) through the membrane, which also depends on molecular diffusion, electro-osmotic drag and convection, can be given by:

$$N_{\text{MLcr}}=-D_{\text{M,N}}\nabla C_{\text{ML}}+n_{\text{d,M}}\frac{I}{F}-\left(\frac{K_{\text{mem}}\Delta p_{\text{l,c-a}}}{\mu_{\text{l}}\delta_{\text{mem}}}\right)C_{\text{ML}} \tag{23}$$

where $\Delta p_{\text{l,c-a}}$ represents the liquid pressure difference between the cathode and the anode.

3.1.4. Energy

The energy equation used in the entire computational domain can be expressed as follows:

$$\frac{\partial((\rho_{\text{g}}c_{\text{p,g}}u_{\text{g}}+\rho_{\text{l}}c_{\text{p,l}}u_{\text{l}})T)}{\partial x}+\frac{1}{r}\frac{\partial(r(\rho_{\text{g}}c_{\text{p,g}}v_{\text{g}}+\rho_{\text{l}}c_{\text{p,l}}v_{\text{l}})T)}{\partial r}=\frac{\partial}{\partial x}\left(k_{\text{T}}^{\text{eff}}\frac{\partial T}{\partial x}\right)+\frac{1}{r}\frac{\partial}{\partial r}\left(rk_{\text{T}}^{\text{eff}}\frac{\partial T}{\partial r}\right)+S_{\text{T}} \tag{24}$$

where $k_{\text{T}}^{\text{eff}}$ represents the effective thermal conductivity of the heat transfer media, and S_{T} denotes the heat generation rate.

3.1.5. Anode flow channel (inside the tube)

Since complicated two-phase flow patterns in the DMFC anode and cathode channels have not yet been established quantitatively, a one-dimensional drift-flux flow model and a homogeneous mist flow model, along the flow direction, are used to describe the two-phase flow in the anode and cathode channels, respectively. The general governing equations of the mass, momentum, species, and energy conservation corresponding to each phase are given by:

$$\textbf{Mass conservation}: \quad \frac{\partial(\rho_{\text{l}}(1-\bar{s}_{\text{g}})\bar{u}_{\text{l}})}{\partial x}=\frac{2m_{\text{l,afc}}}{r_1} \tag{25}$$

$$\frac{\partial(\rho_{\text{g}}\bar{s}_{\text{g}}\bar{u}_{\text{g}})}{\partial x}=\frac{2m_{\text{g,afc}}}{r_1} \tag{26}$$

where $\bar{s}_{\text{g}}$ represents the cross-sectional averaged gas void fraction in the anode channel, $\bar{u}_{\text{l}}$ and $\bar{u}_{\text{g}}$ denote the cross-sectional averaged velocities of the liquid and gas phases, respectively, and $m_{\text{l,afc}}$ and $m_{\text{g,afc}}$ represent the liquid and gas mass fluxes at the interface ($r = r_1$) toward the anode channel.

$$\textbf{Momentum equation}: \quad \frac{\partial(\rho_{\text{l}}(1-\bar{s}_{\text{g}})\bar{u}_{\text{l}}\bar{u}_{\text{l}})}{\partial x}+\frac{\partial(\rho_{\text{g}}\bar{s}_{\text{g}}\bar{u}_{\text{g}}\bar{u}_{\text{g}})}{\partial x}=-\frac{\partial\bar{p}_{\text{m}}}{\partial x}-2\rho_{\text{m}}\frac{f_{\text{m}}}{D_{\text{h,afc}}}\bar{u}_{\text{m}}\left|\bar{u}_{\text{m}}\right| \tag{27}$$

Table 1
Boundary conditions for the tubular DMFC model.

Location	Variables	Mass/molar flux	Heat flux
$r=r_1$	$p_l\|_+ = \bar{p}_m$, $s_l\|_+ = (1-\bar{s}_g)$,	$m_l\|_+ = m_{l,afc}$	$q\|_+ = q_{afc}$
	$C_{ML}\|_+ = \bar{C}_{MeOH}$,,	$m_g\|_+ = m_{g,afc}$	
	$T\|_+ = q_{afc}/h_{Ta} + \bar{T}_{afc}$	$N_{MeOH}\|_+ = N_{MeOH,afc}$	
		$N_i\|_+ = N_{i,afc}$	
$r=r_4$	$\frac{\partial p_l}{\partial r}\Big\|_- = 0$, $\frac{\partial p_g}{\partial r}\Big\|_- = 0$,	$m_l\|_- = 0$	$q\|_- = q\|_+$
	$\lambda^*_{we}\Big\|_+ = \lambda^*_{we,v} + (\lambda^*_{we,l} - \lambda^*_{we,v})s\|_-$	$m_g\|_- = 0$	
		$N_i\|_- = 0$	
$r=r_5$	$C_{MeOH}\|_+ = 0$, $\frac{\partial p_l}{\partial r}\Big\|_+ = 0$,	$m_l\|_+ = 0$	$q\|_- = q\|_+$
	$\frac{\partial p_g}{\partial r}\Big\|_+ = 0$,	$m_g\|_+ = 0$	
	$\lambda^*_{we}\Big\|_- = \lambda^*_{we,v} + (\lambda^*_{we,l} - \lambda^*_{we,v})s\|_+$	$N_i\|_+ = 0$	
$r=r_8$	$p_g\Big\|_- = \bar{p}_m$, $s_l\|_- = (1-\bar{s}_g)$,	$m_l\|_- = m_{l,cfc}$	$q\|_- = q_{cfc}$
	$C_{O_2,gc}\Big\|_- = \bar{C}_{O_2,cfc}$,,	$m_g\|_- = m_{g,cfc}$	
	$T\|_- = q_{cfc}/h_{Tc} + \bar{T}_{cfc}$	$N_i\|_- = N_{i,cfc}$	
$0<r<r_1$ and $(x=0)$	$\bar{C}_{MeOH}\Big\|_+ = C_{MeOH,in}$, $\bar{p}_m\|_+ = 1$ atm		
	$T = T_{in}$, $\bar{u}_l\|_+ = u_{a,in}$, $\bar{s}_g\Big\|_+ = 0$		
$r_8<r<r_9$ and $(x=0)$	$\bar{C}_{O_2}\Big\|_+ = C_{O_2,in}$, $\bar{C}_{WV}\Big\|_+ = C_{WV,in}$,		
	$\bar{p}_m\|_+ = 1$ atm, $T = T_{in}$		
	$\bar{u}_g\Big\|_+ = u_{c,in}$, $\bar{s}_l\|_+ = 0$		
$r_1<r<r_8$ and ($x=0$ or $x=L$)	$\frac{\partial p_l}{\partial r}\Big\|_+ = 0$, $\frac{\partial p_g}{\partial r}\Big\|_+ = 0$	$m_l\|_+ = 0$	$q\|_+ = 0$
		$m_g\|_+ = 0$	
		$N_i\|_+ = 0$	
		$N_{MeOH}\|_+ = 0$	

where $\bar{p}_m$ represents the pressure inside the anode channel, and $\bar{u}_m$ represents the volumetric velocity of the liquid–gas mixture, and is defined as:

$$\bar{u}_m = \bar{u}_l(1-\bar{s}_g) + \bar{u}_g\bar{s}_g \tag{28}$$

The relation between the gas velocity and liquid velocity is defined by the drift-flux model [11,12]:

$$\bar{u}_g = C_0\bar{u}_m + \bar{u}_{gj} \tag{29}$$

where the distribution parameter, $C_0 = (1.2 - 0.2\sqrt{\rho_g/\rho_l})(1 - e^{-18.0\bar{s}_g})$, and the drift velocity, $\bar{u}_{gj} = 0.37\sqrt{2r_1(\rho_l-\rho_g)\vec{g}/\rho_l}$, are suitable for a bubbly flow in a pipe [35].

Species :
$$\frac{\partial((1-\bar{s}_g)\bar{u}_l\bar{C}_{MeOH})}{\partial x} = \frac{2N_{MeOH,afc}}{r_1} \tag{30}$$

$$\frac{\partial(\bar{s}_g\bar{u}_g\bar{C}_{i,afc})}{\partial x} = \frac{2N_{i,afc}}{r_1} \tag{31}$$

where $N_{i,afc}$ represents the molar flux of the species (i.e., $C_{ML,a}$, $C_{MV,ga}$, $C_{WA,ga}$) at the interface ($r=r_1$) toward the anode channel.

Energy :
$$\frac{\partial((\rho_g c_{p,g}u_g + \rho_l c_{p,l}u_l)\bar{T}_{afc})}{\partial x} = \frac{2q_{T,afc}}{r_1} \tag{32}$$

where $\bar{T}_{afc}$ represents the cross-sectional averaged temperature of the mixture, and $q_{T,afc}$ represents the heat flux at the interface ($r=r_1$) toward the anode channel.

3.1.6. Cathode channel (outside the tube)

Similar to the anode, the governing equations for the homogeneous mist flow in the cathode channel are listed as follows:

Mass conservation :
$$\frac{\partial(\rho_l\bar{s}_l\bar{u}_l)}{\partial x} = \frac{2r_8m_{l,cfc}}{(r_9^2-r_8^2)} \tag{33}$$

$$\frac{\partial(\rho_g(1-\bar{s}_l)\bar{u}_g)}{\partial x} = \frac{2r_8m_{g,cfc}}{(r_9^2-r_8^2)} \tag{34}$$

Momentum equation :
$$\frac{\partial(\rho_l\bar{s}_l\bar{u}_l\bar{u}_l)}{\partial x} + \frac{\partial(\rho_g(1-\bar{s}_l)\bar{u}_g\bar{u}_g)}{\partial x} = -\frac{\partial\bar{p}_m}{\partial x} - 2\rho_m\frac{f_m}{D_{h,cfc}}\bar{u}_m\left|\bar{u}_m\right| \tag{35}$$

Species :
$$\frac{\partial((1-\bar{s}_l)\bar{u}_g\bar{C}_{i,cfc})}{\partial x} = \frac{2r_8N_{i,cfc}}{(r_9^2-r_8^2)} \tag{36}$$

Energy :
$$\frac{\partial((\rho_g c_{p,g}u_g + \rho_l c_{p,l}u_l)\bar{T}_{cfc})}{\partial x} = \frac{2r_8q_{T,cfc}}{(r_9^2-r_8^2)} \tag{37}$$

3.2. Sub-models

In the anode of the DMFC, the kinetics of the methanol oxidation reaction (MOR) is modeled by the widely used Tafel-like expression:

$$j_a = A_{v,a}j^{ref}_{0,MeOH}\left(\frac{C_M}{C^{ref}_{MeOH}}\right)^{\gamma}\exp\left(\frac{\alpha_a F}{RT}\eta_a\right) \tag{38}$$

where the reaction order (γ) is related to the methanol concentration and is assumed to be zero order when the methanol

Table 2
Constitutive relations in the governing equations for the tubular DMFC model.

Parameters	Expressions
Relative permeabilities	$k_{rl} = s^{4.5}$ Liquid $k_{rg} = (1-s)^{4.5}$ Gas
Effective diffusion coefficients of species	$D_{i,g}^{eff} = D_{i,g}\varepsilon^{1.5}(1-s)^{1.5}$ i : O_2, WV, MV $D_{ML,a}^{eff} = \begin{cases} \frac{D_{M,l}\varepsilon^{1.5}s^{1.5}(\varepsilon+\varepsilon_e)}{[\varepsilon/(D_{M,l}\varepsilon^{1.5}s^{1.5})+\varepsilon_e/(D_{M,N}\varepsilon_e^{1.5})]D_{M,N}} & \text{(ADL(AMPL)/ACL/PEM)} \end{cases}$
Effective thermal conductivity in the porous regions	$k_T^{eff} = \begin{cases} \varepsilon s k_l + \varepsilon(1-s)k_g + k_{DL/MPL/CL} & \text{(DL(MPL,CL)/PEM)} \\ k_{mem} \end{cases}$
Generation rate of mass in liquid phase	$\dot{m}_{l,a} = \begin{cases} M_{H_2O}\tilde{R}_{vl} - M_M\tilde{R}_{MV,ga} \\ M_{H_2O}\left(\tilde{R}_{vl} - \frac{N_{H_2Ocr}}{\delta_{acl}} - \frac{j_a}{6F}\right) - M_M\left(\tilde{R}_{MV,ga} + \frac{j_a}{6F} + \frac{I_p}{6F\delta_{acl}}\right) \end{cases}$ (ADL(AMPL)/ACL) $\dot{m}_{l,c} = \begin{cases} M_{H_2O}\tilde{R}_{vl} \\ M_{H_2O}\left(\tilde{R}_{vl} + \frac{N_{H_2Ocr}}{\delta_{ccl}} + \frac{(j_c - I_p/\delta_{ccl})}{2F} + \frac{I_p}{3F\delta_{ccl}}\right) \end{cases}$ (CDL(CMPL)/CCL)
Generation rate of mass in gas phase	$\dot{m}_{g,a} = \begin{cases} -M_{H_2O}\tilde{R}_{vl} + M_M\tilde{R}_{MV,ga} \\ -M_{H_2O}\tilde{R}_{vl} + M_M\tilde{R}_{MV,ga} + M_{CO_2}\dot{R}_{CO_2,ga} \end{cases}$ (ADL(AMPL)/ACL) $\dot{m}_{g,c} = \begin{cases} -M_{H_2O}\tilde{R}_{vl} \\ -M_{O_2}j_c/4F + M_{CO_2}I_p/6F\delta_{ccl} - M_{H_2O}\tilde{R}_{vl} \end{cases}$ (CDL(CMPL)/CCL)
Mole generation rate of species	$\dot{R}_{O_2,gc} = \begin{cases} 0 \\ -j_c/4F \end{cases}$, $\dot{R}_{WV,gc} = -\tilde{R}_{vl}$ (CDL(CMPL)/CCL) $\dot{R}_{ML,a} = \begin{cases} -\tilde{R}_{MV,ga} \\ -\tilde{R}_{MV,ga} - j_a/6F \end{cases}$ (ADL(AMPL)/ACL) $\dot{R}_{WV,ga} = -\tilde{R}_{vl}$, $\dot{R}_{MV,ga} = \tilde{R}_{MV,ga}$ (ADL(AMPL)/ACL)
Heat generation rate	$S_T = \begin{cases} \tilde{R}_{vl}\Delta h_v - \tilde{R}_{MV,g}\Delta h_{Mv} & \text{ADL(AMPL)} \\ j_a(\eta_a - T\Delta S_{MOR}/6F) + I^2/\sigma_{mem}^{eff} + \tilde{R}_{vl}\Delta h_v - \tilde{R}_{MV,g}\Delta h_{Mv} & \text{ACL} \\ I^2/\sigma_{mem} & \text{PEM} \\ j_c(\lvert\eta_c\rvert - T\Delta S_{ORR}/4F) - I_pT\Delta S_{MOR}/6F\delta_{ccl} & \text{CCL} \\ \quad + I^2/\sigma_{mem}^{eff} + \tilde{R}_{vl}\Delta h_v & \\ \tilde{R}_{vl}\Delta h_v & \text{CDL(CMPL)} \end{cases}$

Table 3
Cell geometric dimensions and operating parameters used in the tubular DMFC model.

Parameters	Symbols	Value	Unit
Tube inner radius	r_1	1.0×10^{-3}	m
Anode DL thickness	$r_2 - r_1$	2.6×10^{-4}	m
Anode MPL thickness	$r_3 - r_2$	0.3×10^{-4}	m
Anode CL thickness	$r_4 - r_3$	0.2×10^{-4}	m
Membrane thickness (Nafion 115)	$r_5 - r_4$	1.25×10^{-4}	m
Cathode CL thickness	$r_6 - r_5$	0.2×10^{-4}	m
Cathode MPL thickness	$r_7 - r_6$	0.3×10^{-4}	m
Cathode DL thickness	$r_8 - r_7$	2.6×10^{-4}	m
Flow channel length	L	5.0×10^{-2}	m
Annular cathode channel size	$r_9 - r_8$	1.0×10^{-3}	m
Fuel/Air inlet temperature	T_{in}	333.15	K
Anode channel inlet pressure	$p_{l,in}$	1.013×10^{-5}	Pa
Cathode channel inlet pressure	$p_{g,in}$	1.013×10^{-5}	Pa
Inlet methanol concentration at anode	$C_{M,in}$	1000	mol m^{-3}
Inlet oxygen concentration at cathode	$C_{O_2,in}$	$0.21\times p_g/RT$	mol m^{-3}
Inlet water vapor concentration at cathode	$C_{WV,in}$	0	mol m^{-3}
Inlet carbon dioxide concentration at cathode	$C_{CO_2,in}$	0	mol m^{-3}
Inlet gas saturation at anode	$\bar{s}_g$	0	–
Inlet liquid saturation at cathode	$\bar{s}_l$	0	–

Table 4
Physicochemical properties used in the tubular DMFC model.

Parameters		Symbols	Value	Unit	Ref.
Porosity, permeability	ADL	ε_{adl}, K_{adl}	0.75, 1.0×10^{-12}	–, m^2	[25]
	AMPL	ε_{ampl}, K_{ampl}	0.3, 2.5×10^{-13}	–, m^2	[25]
	ACL	ε_{acl}, K_{acl}	0.3, 1.5×10^{-14}	–, m^2	[25]
	MEM	ε_{mem}, K_{mem}	0.3, 2.0×10^{-18}	–, m^2	[25]
	CCL	ε_{ccl}, K_{ccl}	0.3, 1.5×10^{-14}	–, m^2	[25]
	CMPL	ε_{cmpl}, K_{cmpl}	0.3, 2.5×10^{-13}	–, m^2	[25]
	CDL	ε_{cdl}, K_{cdl}	0.75, 1.0×10^{-12}	–, m^2	[25]
Nafion volume fraction	ACL	$\varepsilon_{e,acl}$	0.3	–	[25]
	CCL	$\varepsilon_{e,ccl}$	0.3	–	[25]
Diffusivities	MeOH in water	$D_{M,l}$	$1.58\times10^{-9}e^{0.02623(T-298)}$	$m^2\,s^{-1}$	[25]
	MeOH in Nafion	$D_{M,N}$	$4.9\times10^{-10}e^{[2436(1/333-1/T)]}$	$m^2\,s^{-1}$	[25]
	Methanol vapor	$D_{M,g}$	$-6.954\times10^{-6}+4.5986\times10^{-8}T+9.4979\times10^{-11}T^2$	$m^2\,s^{-1}$	[25]
	O_2 in gas	$D_{O_2,gc}$	$1.775\times10^{-5}\left(\frac{T}{273.15}\right)^{1.823}$	$m^2\,s^{-1}$	[25]
	Water vapor	$D_{WV,g}$	$2.56\times10^{-5}\left(\frac{T}{307.15}\right)^{2.334}$	$m^2\,s^{-1}$	[25]
	Dissolved water in Nafion	D_{we}	$4.17\times10^{-8}\lambda(161e^{-\lambda}+1)e^{-2436/T}$	$m^2\,s^{-1}$	[25]
Thermal conductivity of membrane		k_{mem}	0.2	$W\,m^{-1}\,K^{-1}$	[29]
Thermal conductivity of DL and CL		k_{DL} (k_{CL})	1.5	$W\,m^{-1}\,K^{-1}$	[29]
Thermal conductivity of MPL		k_{MPL}	1.5	$W\,m^{-1}\,K^{-1}$	[29]
Thermal conductivity of gas		k_g	0.026	$W\,m^{-1}\,K^{-1}$	–
Thermal conductivity of liquid		k_l	0.62	$W\,m^{-1}\,K^{-1}$	–
Heat capacity of liquid water		c_{pl}	4200	$J\,kg^{-1}\,K^{-1}$	–
Heat capacity of gas		c_{pg}	1007	$J\,kg^{-1}\,K^{-1}$	–
Viscosity of gas phase		μ_g	2.03×10^{-5}	$kg\,m^{-1}\,s^{-1}$	[11]
Viscosity of liquid phase		μ_l	4.05×10^{-4}	$kg\,m^{-1}\,s^{-1}$	[11]
Absolute entropy of liquid methanol (1 atm, 298 K)		$\bar{s}^0_{MeOH,l}$	126.8	$J\,mol^{-1}\,K^{-1}$	–
Absolute entropy of liquid water (1 atm, 298 K)		$\bar{s}^0_{H_2O,l}$	69.95	$J\,mol^{-1}\,K^{-1}$	–
Absolute entropy of CO_2 (1 atm, 298 K)		$\bar{s}^0_{CO_2}$	213.685	$J\,mol^{-1}\,K^{-1}$	–
Absolute entropy of O_2 (1 atm, 298 K)		$\bar{s}^0_{O_2}$	205.033	$J\,mol^{-1}\,K^{-1}$	–
Electro-osmotic drag coefficients of water and methanol		n_{d,H_2O}	$\frac{2.5}{22}\lambda$	–	[25]
		$n_{d,M}$	$n_{d,H_2O}x_M$	–	[25]
Evaporation rate constant for water		k_e	5	$(atm\,s)^{-1}$	Assumed
Condensation rate constant for water		k_c	5.0×10^4	s^{-1}	Assumed
Interfacial transfer rate constant for methanol		h_{lg}	0.05	$m^2\,s^{-1}$	[11]
Specific interfacial area between liquid and gas		A_{lg}	10^5	m^{-1}	[11]
Proton conductivity in membrane		σ_{mem}	$7.3e^{[1268(1/298-1/T)]}$	$\Omega^{-1}\,m^{-1}$	[25]
Henry law constant for methanol		$k_{H,M}$	$0.096e^{0.04511(T-273)}$	atm	[25]
The saturation pressure of water vapor		$\log_{10}p^{sat}_{WV}$	$-2.1794+0.02953(T-273)$ $-9.1837\times10^{-5}(T-273)^2$ $+1.4454\times10^{-7}(T-273)^3$	atm	[11]
The saturation pressure of methanol vapor		p^{sat}_{MV}	$k_Hx_{M,l}$	atm	[11]
Latent heat of methanol evaporization		Δh_{Mv}	37.7×10^3	$J\,mol^{-1}$	–
Latent heat of water evaporization		Δh_v	44.9×10^3	$J\,mol^{-1}$	–
Thermodynamic voltage		V_0	1.21	V	[25]
Transfer coefficient of anode		α_a	0.52	–	[25]
Transfer coefficient of cathode		α_c	1.0	–	[25]
Anode exchange current density		$A_{v,a}j^{ref}_{0,M}$	$1\times10^5\ \exp\left(\frac{35570}{R}\left(\frac{1}{353}-\frac{1}{T}\right)\right)$	$A\,m^{-3}$	[25,29]
Cathode exchange current density		$A_{v,c}j^{ref}_{0,O_2}$	$2111\ \exp\left(\frac{73200}{R}\left(\frac{1}{353}-\frac{1}{T}\right)\right)$	$A\,m^{-3}$	[29]
Anode reference concentration		C^{ref}_M	100	$mol\,m^{-3}$	[12]
Cathode reference concentration		$C^{ref}_{O_2}$	36.5	$mol\,m^{-3}$	[11]
Surface tension		σ	0.0644	$N\,m^{-1}$	[25]
Equivalent weight of ionomer		EW	1.1	$kg\,mol^{-1}$	[11]
Dry membrane density		ρ_{dry}	1980	$kg\,m^{-3}$	[11]
Contact resistance		$R_{contact}$	0.45	$\Omega\,cm^2$	Assumed

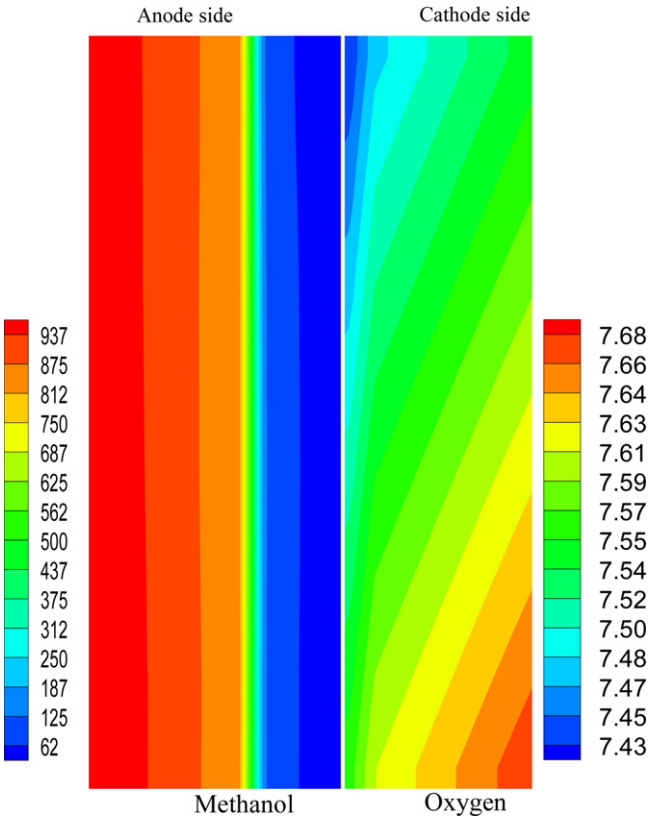

Fig. 4. Distribution of methanol concentration in the anode electrode and membrane and oxygen concentration in the cathode electrode (methanol solution: 1 M; current density: 120 mA cm^{-2}; anode flow rate: 0.015 m s^{-1}; cathode flow rate: 1.0 m s^{-1}).

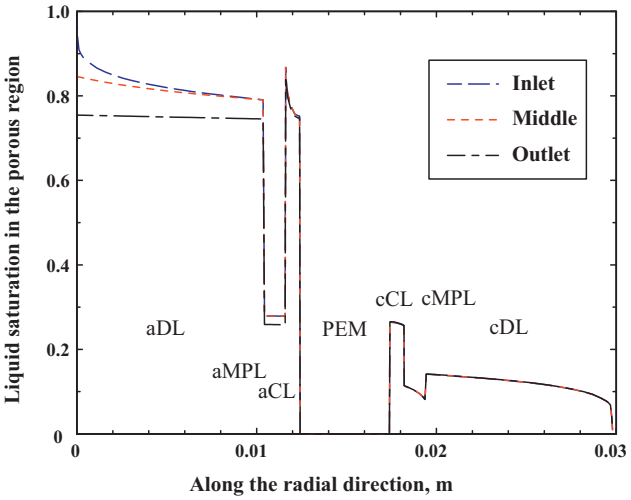

Fig. 6. Distribution of liquid saturation in the porous region at different channel positions (methanol solution: 1 M; current density: 120 mA cm^{-2}; anode flow rate: 0.015 m s^{-1}; cathode flow rate: 1.0 m s^{-1}).

concentration is higher than a reference value [12]. Otherwise, the first-order reaction is applied.

The cell current density can be calculated by

$$I = \int_{\mathrm{ACL}} j_{\mathrm{a}}\, \mathrm{d}x \tag{39}$$

The rate of methanol crossover is expressed by the 'parasitic' current density:

$$I_{\mathrm{p}} = 6FN_{\mathrm{MLcr}} \tag{40}$$

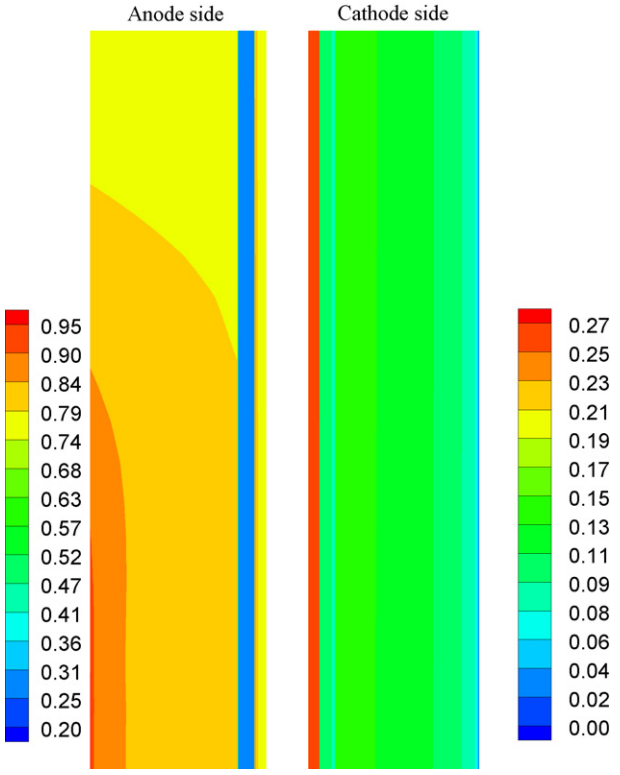

Fig. 5. Distribution of liquid saturation in the porous region (methanol solution: 1 M; current density: 120 mA cm^{-2}; anode flow rate: 0.015 m s^{-1}; cathode flow rate: 1.0 m s^{-1}).

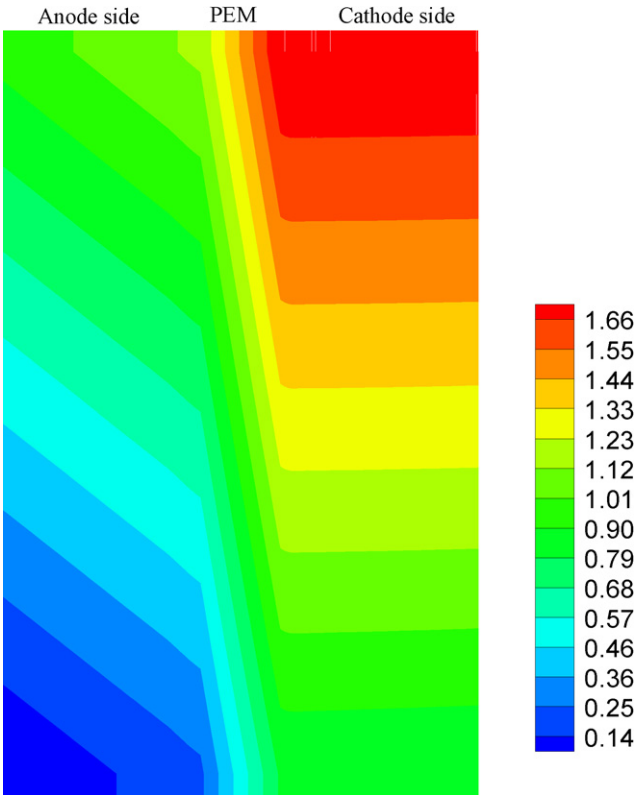

Fig. 7. Distribution of cell temperature rise (methanol solution: 1 M; current density: 120 mA cm^{-2}; anode flow rate: 0.015 m s^{-1}; cathode flow rate: 1.0 m s^{-1}).

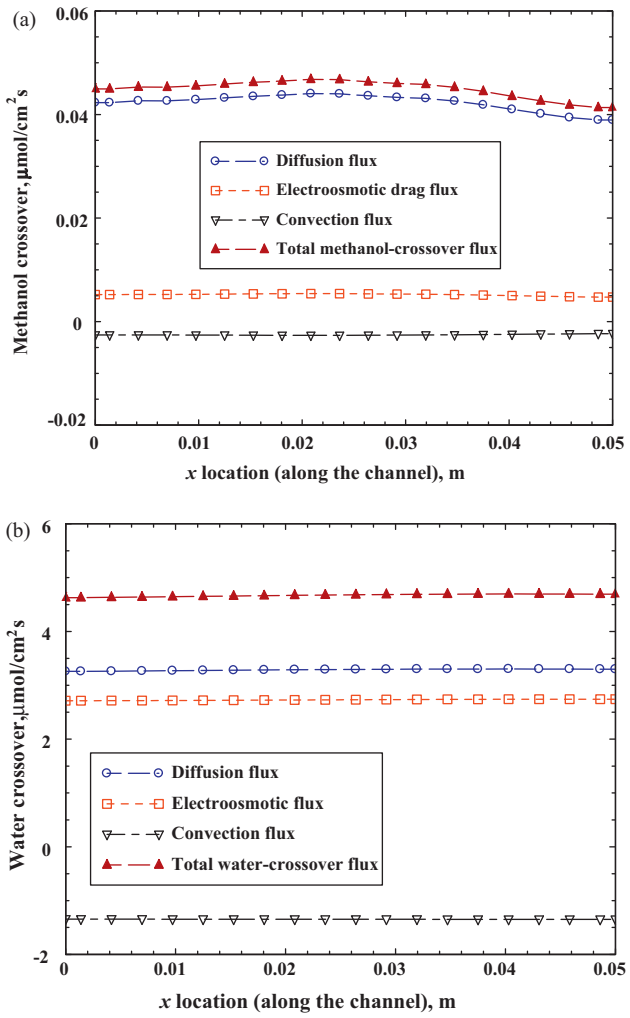

Fig. 8. Axial distributions of fluxes of (a) methanol crossover and (b) water crossover (methanol solution: 1 M; current density: 120 mA cm^{-2}; anode flow rate: 0.015 m s^{-1}; cathode flow rate: 1.0 m s^{-1}).

where the molar flux of methanol crossover, N_{MLcr}, is given by Eq. (23).

On the cathode, it is assumed that both the cell current and 'parasitic' current are entirely consumed by the oxygen reduction reaction (ORR), i.e.:

$$I + I_p = \int_{CCL} j_c \, dx \tag{41}$$

where the ORR is also given by the Tafel-like expression:

$$j_c = (1-s)A_{v,c} j^{ref}_{0,O_2} \left(\frac{C_{O_2}}{C^{ref}_{O_2}}\right) \exp\left(\frac{\alpha_c F}{RT}\eta_c\right) \tag{42}$$

Finally, the cell voltage can be determined from:

$$V_{Cell} = V_0 - \eta_a - \eta_c - I\left(R_{Contact} + \frac{\delta_{mem}}{\sigma_{mem}}\right) \tag{43}$$

where V_0, $R_{Contact}$ and σ_{mem} present the thermodynamic equilibrium voltage of the DMFC, the contact resistance, and the proton conductivity of the membrane, respectively.

For the phase change between liquid water and water vapor, the rate of condensation and evaporation can be modeled using the finite-rate approach [11,25]:

$$\tilde{R}_{vl} = h_{vl}(y_{WV}p_g - p^{sat}_{WV}) \tag{44}$$

where p^{sat}_{WV} is the saturation pressure of water vapor, and y_{WV} is the molar fraction of water vapor in the gas phase. The mass-transfer coefficient (h_{vl}) can be given by:

$$h_{vl} = \frac{k_c \varepsilon (1-s) y_{WV}}{2RT}\left(1 + \frac{|y_{WV}p_g - p^{sat}_{WV}|}{y_{WV}p_g - p^{sat}_{WV}}\right) + \frac{k_e \varepsilon s \rho_l}{2M_{H_2O}}\left(1 - \frac{|y_{WV}p_g - p^{sat}_{WV}|}{y_{WV}p_g - p^{sat}_{WV}}\right) \tag{45}$$

where k_c and k_e are the condensation and evaporation rate constants.

The rate of methanol condensation and evaporation between the liquid phase and vapor phase is modeled by the following expression:

$$\tilde{R}_{MV,g} = A_{lg} h_{lg} s(1-s)\frac{(p^{sat}_{MV} - p_{MV})}{RT} \tag{46}$$

where p^{sat}_{MV} is the saturation pressure of methanol vapor.

Up to this point, the formulation of two-phase mass transport in all of the regions of the tubular DMFC has been presented. To solve the above equations, boundary conditions and additional constitutive correlations are needed, which are described in Tables 1 and 2, respectively. The cell geometric dimensions and operating parameters are listed in Table 3, and the electrochemical properties are listed in Table 4. A simulation code, which was based on the SIMPLER algorithm with the finite-volume method [3,25], was written for the above-described governing equations and boundary conditions. It should be noted that both the main physical framework and the electrochemical parameters used in the present model are based mainly on previous well-developed two-phase models for planar DMFCs [3,25]. The grid independence of the present simulation model has also been fully investigated.

4. Results and discussion

4.1. Detailed information

The distributions of several species, including methanol concentration, oxygen concentration, liquid saturation, and temperature, at a current density of 120 mA cm^{-2} for 1 M solution are presented in Figs. 4–7. The methanol solution and oxygen are fed at velocities of 0.015 and 1.0 m s^{-1}, respectively. Fig. 4 shows the methanol concentration distribution in the anode porous region and the membrane, as well as the oxygen concentration distribution in the cathode porous region. It can be seen that, due to the electrochemical consumption in the anode CL and the methanol crossover from the anode to the cathode through the membrane, the methanol concentration decreases sharply from the surface of the anode DL to the anode CL. While along the flow direction in the channel, the methanol concentration only shows a very slight decrease, which indicates that the anode flow rate is large enough to maintain a uniform distribution of methanol along the flow direction. Due to the oxygen consumption in the cathode CL, the oxygen concentration is decreased from the channel to the cathode CL, and from the inlet to the outlet. Due to the rather low oxygen transport resistance in the gas phase, the decrease in oxygen concentration from the channel to the CL is relatively small.

Fig. 5 shows the liquid saturation distribution at both the anode and the cathode sides. For the anode side, the liquid saturation is relatively large especially in the anode DL and CL (~0.7–0.95), while in the anode MPL, the liquid saturation is rather small (~0.2) due to its high hydrophobicity and low permeability. In each layer, the liquid saturation is higher in the region close to the channel and lower in the region close to the membrane. That is because carbon dioxide

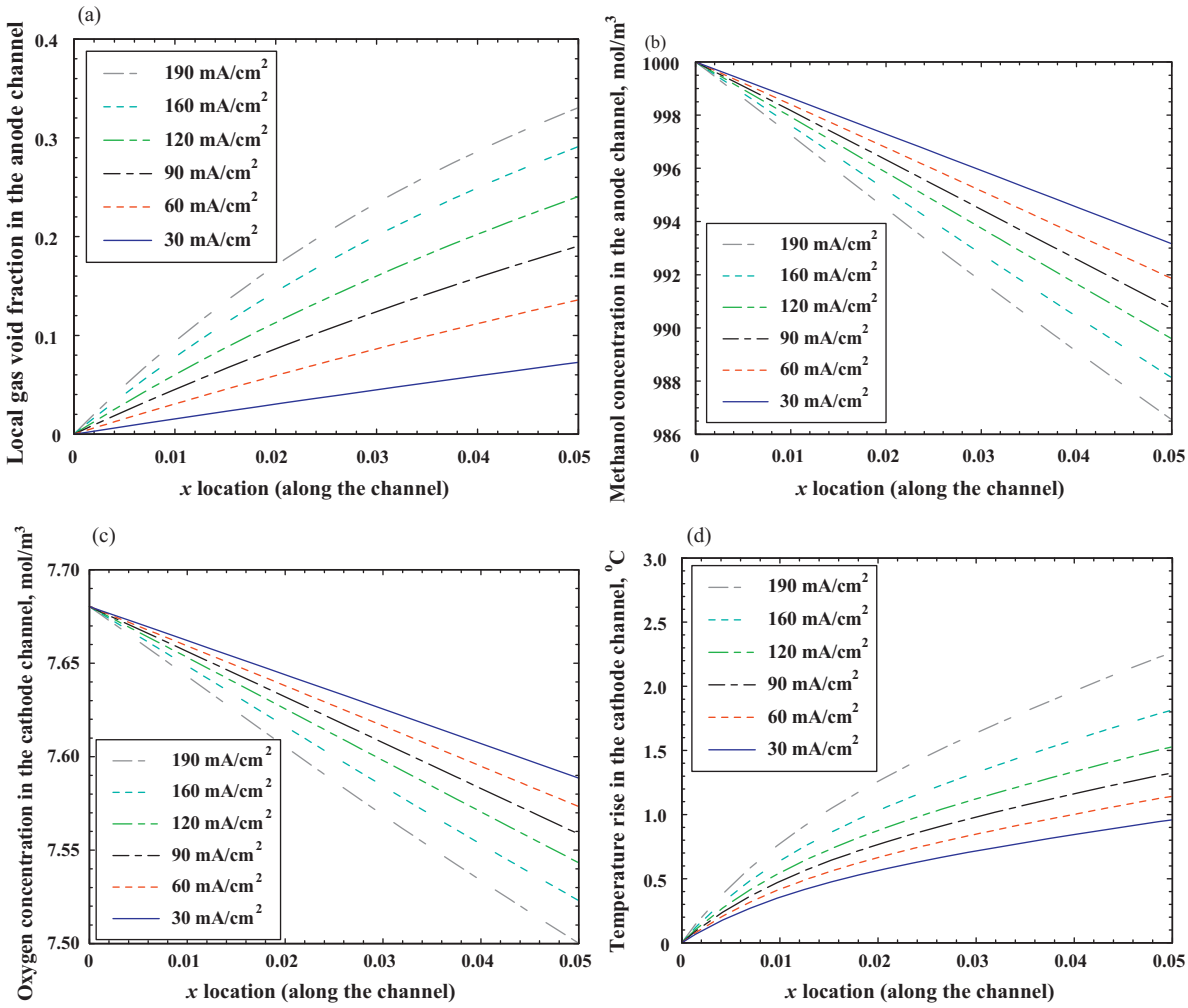

Fig. 9. Variations in cross-sectional averaged (a) gas void fraction in the anode channel, (b) methanol concentration in the anode channel, (c) oxygen concentration in the cathode channel, and (d) temperature rise in the cathode channel along the channel length for various current densities.

gas generated in the anode CL is transported from the anode CL to the channel, and is swept along the channel by the liquid flow. Due to the gas accumulation, the liquid saturation is evidently decreased along the channel direction. The accumulation of carbon dioxide gas may significantly hinder the methanol supply from the channel to the anode CL. For the cathode side, the liquid saturation is rather small, especially in the cathode MPL and DL (<0.2). Accordingly, the oxygen transport resistance is rather small. The liquid saturation distribution and the discontinuity at the interfaces between different porous layers in this tubular DMFC are similar to that of a planar DMFC, as shown by Xu et al. [25]. Also, contrary to the liquid saturation in the anode side, it is seen that there is no evident difference in the liquid saturation between the inlet and outlet region, which means that liquid water can be effectively swept out of the cathode by the air flow through the cathode channel. Previous findings can also be clearly seen by plotting the radial distribution of liquid saturation at different channel positions (i.e., inlet, middle, and outlet), as shown in Fig. 6.

The temperature rise distribution across the whole MEA is presented in Fig. 7. As can be seen, the temperature increases slightly along the flow direction due to the heat generation associated with the electrochemical reaction. Moreover, the temperature in the cathode side is generally larger than that in the anode side. For instance, the temperature rise in the anode DL increases from 0.14 to 0.9 °C from the inlet region to the outlet region, while it increases from about 0.8 to 1.66 °C in the cathode DL. That is because, due to the much higher heat transfer coefficient of liquid flow than gas flow, heat can be removed more effectively through the anode side.

Fig. 8 presents the axial distributions of methanol and water crossovers through the membrane from the anode to the cathode at the same operating conditions as Figs. 4–7. Both the methanol and water crossovers are driven by diffusion, electro-osmosis, and pressure gradient caused convection. As shown in Fig. 8a, the methanol crossover is dominated by the diffusion, and the diffusion flux accounts for about 95% of the total methanol crossover. The convection flux is negative, indicating that the pressure gradient caused convection is from the cathode to the anode. Due to the relatively low methanol concentration in the membrane, the convection flux is rather small. However, it is worth noting that the convection flux may be significantly enhanced by adjusting the cathode structure, and thus, the total methanol crossover can be evidently lowered. On the other hand, the methanol crossover increases slightly and then decreases slightly along the flow direction. That is because along the flow direction, the methanol concentration is decreased, leading to a decreased methanol crossover, while the temperature is increased, leading to an increased diffusivity and hence, methanol crossover. The trade-off of these two effects results in the arch-shaped methanol crossover distribution.

Different from the rather small flux of methanol crossover, the flux of water crossover, as shown in Fig. 8b is much larger. Also, although the water crossover flux is dominated by both diffusion and electro-osmosis, the effect of convection on the total water

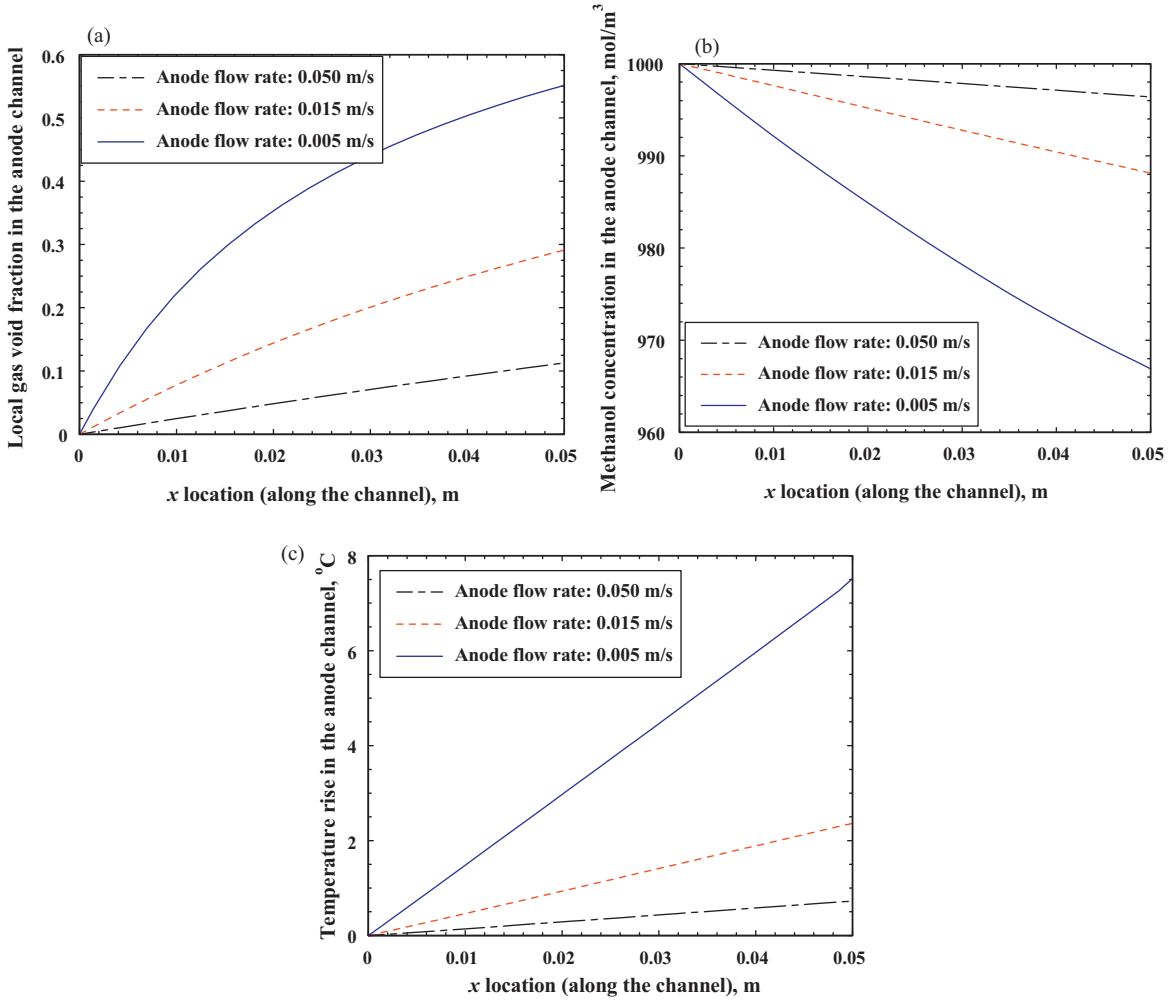

Fig. 10. Variations in cross-sectional averaged (a) gas void fraction in the anode channel, (b) methanol concentration in the anode channel, and (c) temperature rise in the anode channel along the channel length for various anode flow rates (methanol solution: 1 M; current density: 160 mA cm^{-2}; cathode flow rate: 1.0 m s^{-1}).

crossover flux becomes considerable. Along the flow direction, the water crossover remains almost the same, which is due to the fact that the species in the CLs, as shown in Figs. 4–7, are almost the same in the axial direction.

The effect of current density on the distributions of species, including the gas void fraction, methanol concentration, oxygen concentration, and temperature rise, in the channels are shown in Fig. 9. Different current densities ranging from 30 to 190 mA cm^{-2} were tested. The distributions of the cross-sectional averaged gas void fraction in the anode channel at different current densities are shown in Fig. 9a. It can be seen that the gas void fraction increases along the flow direction. For instance, it increases from 0% to 24% from the inlet to the outlet for the current density of 120 mA cm^{-2}. With the increase in the current density, due to the increased carbon dioxide generation, the gas void fraction at the same axial location increases nearly linearly: it increases from about 7% to 33% at the outlet when the current density is increased from 30 to 190 mA cm^{-2}. Clearly, the increased gas void fraction decreases the area for the mass transport of the liquid methanol solution, which reduces the methanol transport from the channel to the anode electrode. The effect of carbon dioxide gas removal on the methanol transport should be well investigated so as to enhance the uniform supply of methanol to the anode CL. It should be noted that, as discovered by Yang et al. [36], the removal of carbon dioxide gas through the channel mainly forms bubbly and slug flow. The present one-dimensional mixture model in the anode channel cannot capture the complex two-phase flow behavior, and thus, more realistic two-phase flow models are needed to better reveal the bubbly flow effect on the methanol transport.

Fig. 9b shows the methanol concentration distributions in the anode channel at different current densities. Due to the electrochemical consumption in the anode CL, the methanol concentration decreases along the flow direction. With the increase in the current density, the methanol concentration also decreases. However, the decrease in the methanol concentration from the inlet to the outlet is rather small, i.e., it decreases only 1.3% at the limiting current density of 190 mA cm^{-2}, which indicates that the present anode flow rate (0.015 m s^{-1}) is large enough to maintain a uniform distribution of methanol along the anode channel. Even at this large methanol flow rate, the gas void fraction in the channel outlet is still considerable, as shown in Fig. 9a. Therefore, the carbon dioxide gas bubbles may affect the methanol transport greatly, and an excessive anode flow rate is needed to avoid severe bubble accumulation in the channel.

Similar to the methanol concentration distribution in the anode channel, the oxygen concentration in the cathode channel, as shown in Fig. 9c, also decreases slightly along the channel due to the electrochemical consumption. A higher current density leads to a larger decrease in oxygen concentration from the inlet to the outlet. Since the liquid saturation is almost zero in the cathode channel (not shown here), and it is relatively small in the cathode DL (as shown in Figs. 5 and 6), the presence of liquid water in the cath-

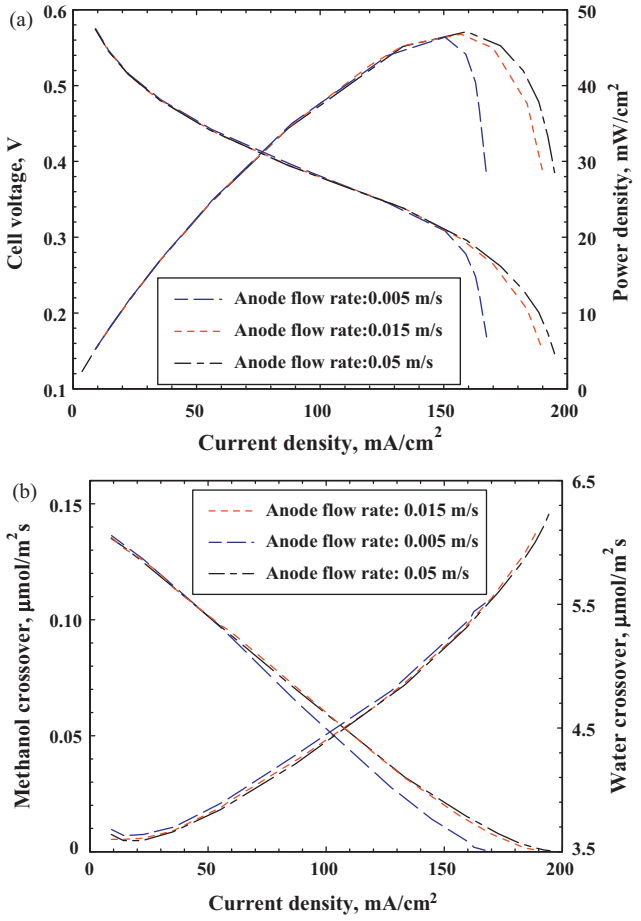

Fig. 11. Variation in the (a) cell voltage, (b) flux of methanol and water crossover through the membrane with current density for various anode flow rates (methanol solution: 1 M; cathode flow rate: 1.0 m s^{-1}).

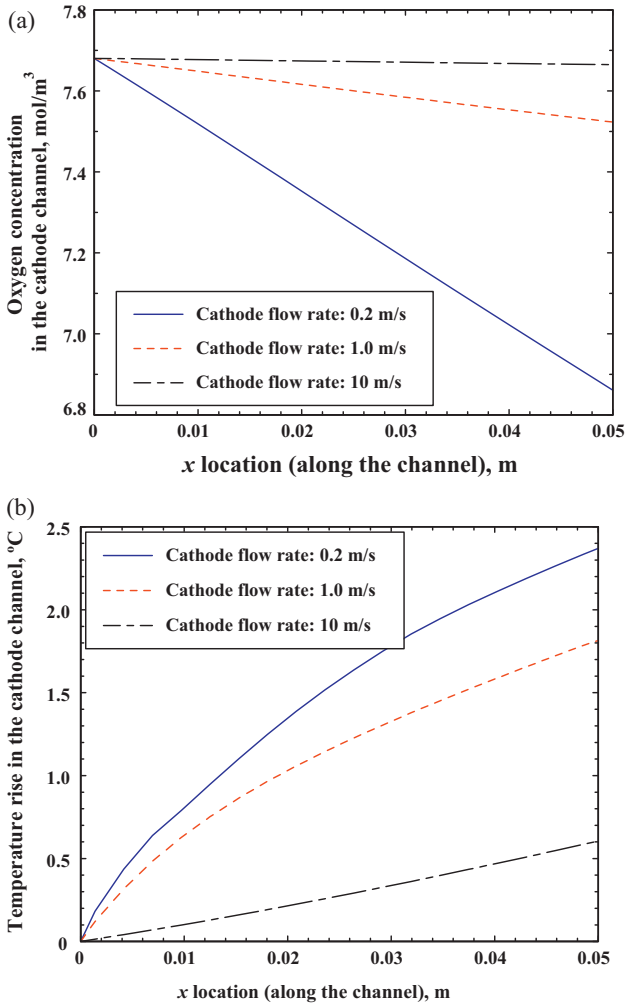

Fig. 12. Variations in cross-sectional averaged (a) oxygen concentration in the cathode channel, (b) temperature rise in the cathode channel along the channel length for various cathode flow rates (methanol solution: 1 M; current density: 160 mA cm^{-2}; anode flow rate: 0.015 m s^{-1}).

ode has a much lesser influence on the oxygen transport when the oxygen is supplied in an active mode. The cross-sectional averaged temperature in the channel also depends on the current density, as can be seen in Fig. 9d for the cathode channel. The cell temperature increases along the flow direction due to the heat generation in the MEA, and the increment becomes larger for higher current densities. For the largest current density of 190 mA cm^{-2}, the temperature in the cathode channel is increased about 2.3 °C from the inlet to the outlet.

4.2. Effect of anode flow rate

The distributions of the cross-sectional averaged methanol concentration, gas void fraction, and temperature rise in the anode channel for various anode flow rates at a current density of 160 mA cm^{-2} are presented in Fig. 10. It can be seen that the methanol concentration (Fig. 10a) decreases with the decrease in the anode flow rate. When the anode flow rate is decreased from 0.05 to 0.005 m s^{-1}, the decrease in the methanol concentration from the inlet to the outlet is increased from about 0.2% to 3.4%. Even for the smallest anode flow rate, the change of methanol concentration is still rather small. On the contrary, the gas void fraction (Fig. 10b) clearly increases with the decrease in the anode flow rate. When the anode flow rate is decreased from 0.05 to 0.005 m s^{-1}, the gas void fraction in the anode channel outlet is significantly increased from about 11% to 55%. That is because less carbon dioxide gas leaves the anode channel during a lower flow rate. Therefore, a large anode flow rate, which may seem excessive for a uniform supply of methanol along the channel, is still necessary to avoid severe gas accumulation in the anode channel which may significantly block the methanol supply to the anode CL. For the temperature rise in the anode channel as shown in Fig. 10c, due to the heat removal by the liquid flow, the temperature is increased along the flow direction. With the decrease in the anode flow rate, the heat removal per unit mass flow is increased, and thus, the temperature is further increased. When the anode flow rate is decreased from 0.05 to 0.005 m s^{-1}, the temperature rise at the channel outlet significantly increases from about 0.7 to 7.5 °C. Therefore, a too low anode flow rate not only results in a severe gas accumulation in the channel, but also leads to a highly non-uniform temperature distribution along the flow direction.

The cell performance, as well as the flux of methanol and water crossovers, for various anode flow rates ranging from 0.05 to 0.005 m s^{-1} is shown in Fig. 11. It is found that the anode flow rate can greatly affect the cell performance. The cell limiting current density increases with the flow rate, which is similar to the results of a planar DMFC [11]. For instance, when the anode flow rate is decreased from 0.05 to 0.005 m s^{-1}, the limiting current density decreases by about 14%. Since the methanol concentration in the channel (Fig. 10a) only decreases by about 3%, the marked decrease in the limiting current density is mainly caused by the significant increase in the gas void fraction in the channel (Fig. 10b), which

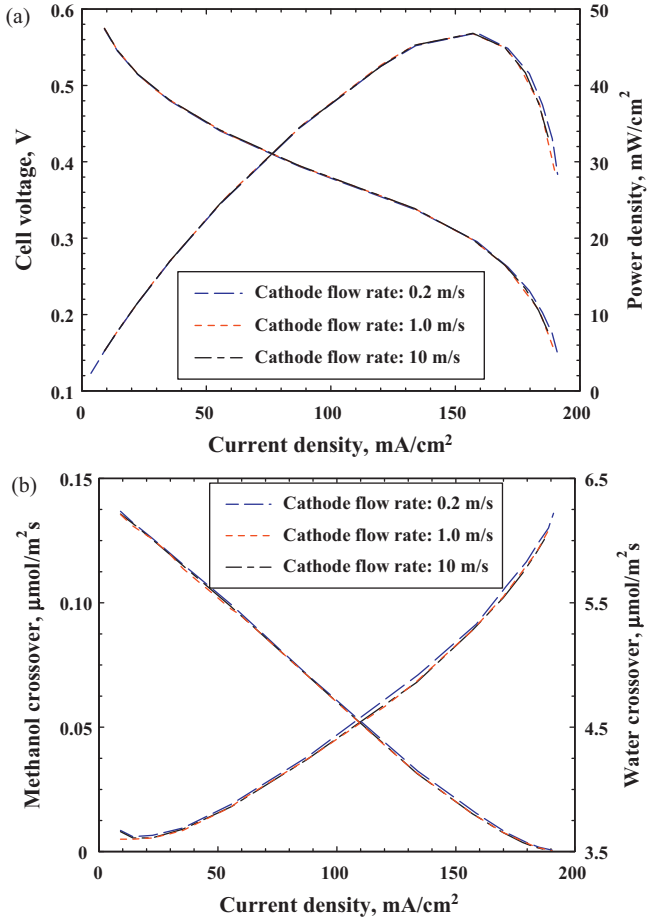

Fig. 13. Variation in the (a) cell voltage, (b) flux of methanol and water crossover through the membrane with current density for various cathode flow rates (methanol solution: 1 M; anode flow rate: 0.015 m s^{-1}).

hinders the methanol transport from the channel to the anode DL. It should be noted that investigating the effect of gas bubbles in the channel on the methanol transport using the present one-dimensional drift-flux model is just an initial approximation, and more realistic investigations need extremely sophisticated two-phase flow modeling in the porous region and the channel.

It is seen in Fig. 11b that the methanol crossover decreases sharply with the current density, and approaches zero at the limiting current density. That is because, with the feeding of 1 M solution, the methanol concentration in the anode CL significantly decreases with the current density, which decreases the methanol diffusion through the membrane. At low current densities, the methanol crossover is almost the same for the different anode flow rates, while at large current densities, the methanol crossover slightly decreases with the decrease in the anode flow rates. That is also due to the blockage effect of gas accumulation in the anode channel on the methanol transport. Also, it is seen that the water crossover increases with the current density. For instance, it increases from about 3.6 to 5.7 μmol cm^{-2} s^{-1} when the current density increases from 0 to 180 mA cm^{-2}. This trend is also similar to that of a planar DMFC, which has been well addressed elsewhere [25]. On the other hand, since the anode flow rates cannot evidently alter the water status in the MEA, the water crossover is almost the same for the different anode flow rates.

4.3. Effect of cathode flow rate

The distributions of the cross-sectional averaged oxygen concentration and temperature rise in the cathode channel for various cathode flow rates at a current density of 160 mA cm^{-2} is presented in Fig. 12. From Fig. 12a, the oxygen concentration decreases along the flow direction due to the electrochemical consumption, and the decrease becomes larger with the decrease in the oxygen flow rate. When the oxygen flow rate is decreased from 10 to 0.2 m s^{-1}, the decrease in the oxygen concentration from the inlet to the outlet is increased from about 0.1% to 11%. For the temperature rise in the cathode channel (Fig. 12b), due to the heat removal by the gas flow, the temperature also increases along the flow direction. With the decrease in the oxygen flow rate, the temperature is further increased. When the oxygen flow rate is decreased from 10 to 0.2 m s^{-1}, the temperature rise at the channel outlet increased from about 0.6 to 2.4 °C. Therefore, a too low oxygen flow rate also leads to a highly non-uniform distribution of temperature along the flow direction.

On the other hand, it should be noted that due to the homogeneous model used in the cathode channel, as well as the Leverett relation used in the cathode porous region, the predicted liquid saturation in the channel (<0.01) and in the cathode porous region (<0.2) is rather small. Accordingly, the effect of liquid water accumulation in the cathode on the oxygen transport is underestimated. Moreover, the change of liquid saturation with oxygen flow rate is also rather small, leading to a negligible influence on the cell performance, as shown in Fig. 13a. It is seen that the cell performance is almost the same for the different oxygen flow rates ranging from 0.2 to 10 m s^{-1}. More accurate modeling depends on the measurement of the capillary property of the cathode porous region, as well as the micro-scale modeling of the two-phase flow. For the methanol and water crossovers as shown in Fig. 13b, it is seen that the fluxes of methanol and water crossovers are all almost independent of the oxygen flow rate. That is because, on the one hand, the methanol crossover mainly depends on the state of the anode side, which is almost unchanged during the increase in the oxygen flow rate. On the other hand, the water saturation in the cathode porous region does not evidently change with the oxygen flow rate, which leads to an unchanged water crossover.

5. Conclusions

Through a simple analysis, it is shown that a tubular DMFC system can yield a higher energy density than a planar DMFC system by properly choosing the tube radius and the distance between adjacent cells. Furthermore, based on a steady state, two-dimensional, two-phase, non-isothermal model, the mass and heat transport characteristics in a tubular DMFC, with different current densities, methanol flow rates and air flow rates, were numerically investigated. The results showed that along the flow direction, the temperature slightly increases, while the temperature in the cathode side is larger than that in the anode side. Due to the trade-off between the decrease in methanol concentration and the increase in temperature, the methanol crossover first increases and then slightly decreases along the flow direction. It is also found that to avoid severe bubble accumulation in the anode channel, a larger, excessive anode flow rate is needed to maintain a uniform distribution of methanol along the anode channel. Lowering the flow rates of the methanol solution or air leads to a higher temperature increase along the flow channel, while resulting in negligible changes in the methanol and water crossovers through the membrane.

Acknowledgement

The financial support from the National Science Foundation (Contract No. CBET-0730349) is gratefully acknowledged.

References

[1] C.K. Dyer, J. Power Sources 106 (2002) 31–34.
[2] C. Xu, T.S. Zhao, J. Power Sources 168 (2007) 143–153.
[3] C. Xu, A. Faghri, Int. J. Heat Mass Transfer 53 (2010) 1951–1956.
[4] C. Xu, A. Faghri, X. Li, T. Ward, Int. J. Hydrogen Energy 35 (2010) 1769–1777.
[5] C. Xu, A. Faghri, X. Li, J. Electrochem. Soc. 157 (2010) B1109–B1117.
[6] X. Li, A. Faghri, C. Xu, Int. J. Hydrogen Energy (2010), doi:10.1016/j.ijhydene.2010.05.033.
[7] B. Xiao, H. Bahrami, A. Faghri, J. Power Sources 195 (2010) 2248–2259.
[8] H. Bahrami, A. Faghri, Int. J. Heat Mass Transfer 53 (2010) 2563–2578.
[9] D. Kim, E.A. Cho, S.-A. Hong, I.-H. Oh, H.Y. Ha, J. Power Sources 130 (2004) 172–177.
[10] Z. Guo, A. Faghri, J. Power Sources 160 (2006) 1183–1194.
[11] W.W. Yang, T.S. Zhao, Electrochim. Acta 52 (2007) 6125–6140.
[12] Z.H. Wang, C.Y. Wang, J. Electrochem. Soc. 150 (2003) A508–A519.
[13] J.G. Liu, T.S. Zhao, R. Chen, C.W. Wong, Electrochem. Commun. 7 (2005) 288–294.
[14] Z. Guo, A. Faghri, J. Power Sources 160 (2006) 1142–1155.
[15] Y. Cao, Proceedings of MNC2007 MicroNanoChina07, January 10–13, 2007, Sanya, Hainan, China, Paper No. MNC2007-21471.
[16] M. Kunimatsu, T. Okada, Electrochem. Solid-State Lett. 7 (2004) A389–A390.
[17] H. Qiao, M. Kunimatsu, N. Fujiwara, T. Okada, Electrochem. Solid-State Lett. 8 (2005) A175–A178.
[18] H. Qiao, M. Kunimatsu, T. Okada, J. Power Sources 139 (2005) 30–34.
[19] H. Qiao, T. Kasajima, M. Kunimatsu, N. Fujiwara, T. Okada, J. Electrochem. Soc. 153 (2006) A42–A47.
[20] Z.G. Shao, W.F. Lin, F.Y. Zhu, P.A. Christensen, H.M. Zhang, B.L. Yi, J. Power Sources 160 (2006) 1003–1008.
[21] Z.G. Shao, W.F. Lin, F.Y. Zhu, P.A. Christensen, H.M. Zhang, Fuel Cells 06 (2006) 326–330.
[22] M.S. Yazici, J. Power Sources 166 (2007) 137–142.
[23] R.J. Yu, G.Y. Cao, X.Q. Liu, Z.F. Li, W. Xing, X.J. Zhu, J. Fuel Cell Sci. Technol. 4 (2007) 520–524.
[24] M.S. Lee, L.J. Chen, M.F. Hung, M.Y. Lo, S.J. Sue, C.H. Lo, Y.P. Wang, J. Fuel Cell Sci. Technol. 5 (2008) 031004.
[25] C. Xu, T.S. Zhao, W.W. Yang, J. Power Sources 178 (2008) 291–308.
[26] W.W. Yang, T.S. Zhao, J. Power Sources 174 (2007) 136–147.
[27] W.P. Liu, C.Y. Wang, J. Electrochem. Soc. 154 (2007) B352–B361.
[28] W.P. Liu, C.Y. Wang, J. Power Sources 164 (2007) 189–195.
[29] R. Chen, T.S. Zhao, W.W. Yang, C. Xu, J. Power Sources 175 (2008) 276–287.
[30] J. Rice, A. Faghri, Int. J. Heat Mass Transfer 49 (2006) 4804–4820.
[31] J. Rice, A. Faghri, J. Heat Transfer 130 (2008) 062001.
[32] M.A.R.S. Al-Baghdadi, Energy Convers. Manage. 49 (2008) 2986–2996.
[33] A. Faghri, Y. Zhang, Transport Phenomena in Multiphase Systems, Elsevier Inc., 2006.
[34] C. Xu, A. Faghri, J. Fuel Cell Sci. Technol. 7 (2010) 061007.
[35] T. Hibiki, M. Ishii, Int. J. Heat Mass Transfer 45 (2002) 707–721.
[36] H. Yang, T.S. Zhao, Q. Ye, J. Power Sources 139 (2005) 79–90.